



Performance characteristics of UV imaging instrumentation for diffusion, dissolution and release testing studies

Jensen, Sabine S; Jensen, Henrik; Goodall, David M; Østergaard, Jesper

Published in:

Journal of Pharmaceutical and Biomedical Analysis

DOI:

[10.1016/j.jpba.2016.08.018](https://doi.org/10.1016/j.jpba.2016.08.018)

Publication date:

2016

Document version

Peer reviewed version

Document license:

[CC BY-NC](https://creativecommons.org/licenses/by-nc/4.0/)

Citation for published version (APA):

Jensen, S. S., Jensen, H., Goodall, D. M., & Østergaard, J. (2016). Performance characteristics of UV imaging instrumentation for diffusion, dissolution and release testing studies. *Journal of Pharmaceutical and Biomedical Analysis*, 131, 113-123. <https://doi.org/10.1016/j.jpba.2016.08.018>

1 **Performance characteristics of UV imaging instrumentation for diffusion, dissolution and**
2 **release testing studies**

3 Sabrine S. Jensen^{a,b}, Henrik Jensen^a, David M. Goodall^c and Jesper Østergaard^{a,*}

4
5 ^aDepartment of Pharmacy, Faculty of Health and Medical Sciences, University of Copenhagen,
6 Universitetsparken 2, DK-2100 Copenhagen, Denmark.

7
8 ^bPresent address: Novo Nordisk A/S, Novo Nordisk Park, DK-2760 Måløv, Denmark.

9
10 ^cParaytec Limited, York House, Outgang Lane, Osbaldwick, York, YO19 5UP, United Kingdom

11
12
13 *Correspondence: Jesper Østergaard. Department of Pharmacy, Faculty of Health and Medical
14 Sciences, University of Copenhagen, Universitetsparken 2, DK-2100 Copenhagen, Denmark. E-
15 mail: jesper.ostergaard@sund.ku.dk, Telephone: +45 3533 6138, Fax: +45 3533 6001

16 *This is a post-peer-review, pre-copyedit version of an article published in Journal of Pharmaceutical and*
17 *Biomedical Analysis.*



19 *The final authenticated version is available online at:* <http://dx.doi.org/10.1016/j.jpba.2016.08.018>

20

21 **Abstract**

22 UV imaging is capable of providing spatially and temporally resolved absorbance measurements,
23 which is highly beneficial in drug diffusion, dissolution and release testing studies. For optimal
24 planning and design of experiments, knowledge about the capabilities and limitations of the
25 imaging system is required. The aim of this study was to characterize the performance of two
26 commercially available UV imaging systems, the D100 and SDI. Lidocaine crystals, lidocaine
27 containing solutions, and gels were applied in the practical assessment of the UV imaging
28 systems. Dissolution of lidocaine from single crystals into phosphate buffer and 0.5% (w/v)
29 agarose hydrogel at pH 7.4 was investigated to shed light on the importance of density gradients
30 under dissolution conditions in the absence of convective flow. In addition, the resolution of the
31 UV imaging systems was assessed by the use of grids. Resolution was found to be better in the
32 vertical direction than the horizontal direction, consistent with the illumination geometry. The
33 collimating lens in the SDI imaging system was shown to provide more uniform light intensity
34 across the UV imaging area and resulted in better resolution as compared to the D100 imaging
35 system (a system without a lens). Under optimal conditions, the resolution was determined to be
36 12.5 and 16.7 line pairs per mm (lp/mm) corresponding to line widths of 40 μm and 30 μm in the
37 horizontal and vertical direction, respectively. Overall, the performance of the UV imaging
38 systems was shown mainly to depend on collimation of light, the light path, the positioning of
39 the object relative to the line of 100 micron fibres which forms the light source, and the distance
40 of the object from the sensor surface.

41

42 **Keywords:** Dissolution imaging; Dissolution testing; Instrument performance; Spatial
43 resolution; UV imaging

44 **Abbreviations:** API, active pharmaceutical ingredient; CARS, coherent anti-Stokes Raman
45 Scattering Microscopy; CMOS, Complementary metal oxide semiconductor; FTIR, Fourier
46 transform infrared; LOD, Limit of detection; MRI, magnetic resonance imaging; TDA, Taylor
47 dispersion analysis.

48

49 **1. Introduction**

50 Dissolution and release testing is conducted for various purposes in the pharmaceutical industry
51 e.g., to guide the drug development process, in quality control, and as biowaivers [1]. In the early
52 phases of drug development, miniaturized or micro-scale techniques requiring low-milligram
53 quantities of the active pharmaceutical ingredient (API) or formulation are of particular value [2-
54 4]. Many dissolution and release testing methods are invasive methods and involve bulk solution
55 concentration measurements by the withdrawal of test samples, which may disturb the
56 subsequent release. In addition, the withdrawal of samples may also lead to delayed responses,
57 due to the need for accumulation of the API in solution. Especially, in case of fast dissolution
58 and release kinetics real-time analysis is advantageous. Better understanding of the dissolution or
59 release behavior of an API or formulation may be attained using imaging techniques providing
60 spatially, spectrally, and/or temporally resolved information. Imaging techniques used in
61 pharmaceutical sciences for investigating drug dissolution and release processes include
62 magnetic resonance imaging (MRI) [5-8], Fourier transform infrared (FTIR) imaging [4, 9-11],
63 coherent anti-Stokes Raman Scattering Microscopy (CARS) imaging [12], fluorescence imaging

64 [13,14], and UV imaging [15,16]. UV imaging is compatible with a small scale format and has
65 attracted attention as it offers insights into dissolution and release processes of drugs [17-27].
66 However, limited data are available regarding system performance of the commercially available
67 UV imaging instrumentation. The current study was prompted by observations made during UV
68 imaging experiments in our lab, and an associated wish to understand better the performance
69 characteristics of the instrumentation, since this knowledge would be useful in the design,
70 planning, and execution of future experiments. The purpose of the present study was to
71 characterize two embodiments of a commercially-available UV imaging system in terms of
72 analytical performance, including spatial resolution, linearity and noise. The instruments subject
73 to study were an SDI (Sirius-Analytical, Forest Row, UK) and a D100 (Paraytec Ltd, York, UK)
74 imaging system.

75

76 **2. Experimental**

77 2.1 Materials and sample preparations

78 Agarose (type I) was obtained from Sigma-Aldrich (St. Louis, MO, USA). Sodium hydroxide
79 and sodium dihydrogenphosphate monohydrate were obtained from Merck (Darmstadt,
80 Germany). Lidocaine (Ph Eur (European Pharmacopoeia) 6th ed.) was obtained from Unikem
81 (Copenhagen, Denmark). Lidocaine crystals were prepared as described previously [16].

82 A 0.067 M phosphate buffered solution with an ionic strength of 0.15 M was prepared as
83 follows. A weighed amount of sodium dihydrogenphosphate monohydrate (9.25 g) was
84 transferred to a 1000 ml volumetric flask to which was then added de-ionized water to the neck

85 of the volumetric flask. The mixture was stirred at room temperature until the substance was
86 dissolved, then the pH adjusted to 7.40 by adding 5 M NaOH.

87 For preparing the agarose hydrogels, a weighed amount of agarose powder, corresponding to
88 0.5% (w/v), was suspended in phosphate buffer at pH 7.4 followed by heating of the agarose
89 suspensions to 98°C for approximately 20 min to dissolve the agarose. The agarose solution
90 (approximately 310 µl) was transferred to a quartz cell (8.0 mm × 1.0 mm × 38 mm (H × W ×
91 L)) (Starna Scientific Ltd, Hainault Essex, UK), and the lid of the cell placed on top of the
92 agarose solution. Each quartz cell containing the agarose solution (the pre-gel) was left at room
93 temperature for at least 0.5 h to ensure complete gelation of the agarose matrix.

94 The grids used for estimation of the resolution consisted of a black image made of silver halides
95 (5 µm print layer thickness) coated on one side of a plastic base of polyester (180 µm thickness).
96 The grids were produced under conditions of 21 °C at 50% humidity (JD Photo-Tools, Oldham,
97 UK). The grids were drawn in AutoCAD software (Autodesk Inc., San Rafael, CA, USA). The
98 width of the lines and the distance between the lines were identical and varied in the range 10 -
99 100 µm in 10 µm increments and then in 20 µm increments in the 100 to 400 µm range.

100

101 2.2 Instrumentation

102 The two imaging systems investigated, both utilizing ActiPix technology, were a D100 (Paraytec
103 Ltd., York, UK) and an SDI (Sirius-Analytical, Forest Row UK). In terms of optical design
104 [28,29], the Sirius SDI has improvements relative to the D100 through incorporating a lens for
105 collimating the light in the direction parallel to the line of 90 x 100 µm optical fibres which

106 provide the 9 mm x 100 μ m illumination source. The UV imaging systems are shown in
107 Supplementary data Fig. S.1. The active pixel CMOS sensors have a total detection area of 9 mm
108 \times 7 mm consisting of 1280 \times 1024 pixels with a size of 7 μ m \times 7 μ m. Band pass filters with a
109 band width of 10 nm were sourced from various manufacturers. Images were recorded and
110 analyzed using ActiPix D100 software version 1.4 (Paraytec Ltd.). Images were recorded with a
111 rate of 0.2 images per second, and the integration time was 10 ms. Pixel intensities were
112 converted into absorbance using the ActiPix D100 software.

113

114 2.3 Methods and measurements

115 2.3.1 Linearity

116 Calibration curves of lidocaine in phosphate buffered solution at pH 7.4 in a concentration range
117 of 5×10^{-6} - 1×10^{-2} M were constructed. Absorbance values of lidocaine solutions were
118 measured in quartz cells with light paths of 1 and 4 mm at a wavelength of 214 or 254 nm using
119 the SDI UV imaging system. The results were compared to results obtained using a conventional
120 spectrophotometer (Shimadzu UV-1700, Shimadzu, Kyoto, Japan) and quartz cuvettes with a 10
121 mm light path.

122

123 2.3.2 Noise

124 Assessment of noise was made from the data recorded while preparing the lidocaine calibration
125 curves in phosphate buffered solution at pH 7.4 using the Sirius SDI imaging system. Lidocaine

126 solutions were flowed through the flow cell with an ActiPix flow-through type dissolution
127 cartridge CADISS-3 (Paraytec Ltd.) at a flow rate of 1.0 ml/min. The pixels were binned 10×1
128 ($x \times y$), the images were obtained at a rate of 1.15 frames per second, and the absorbance was
129 read from 5 effective pixel units positioned at different positions in the imaging area.

130

131 2.3.3 Resolution measurement using grids

132 Resolution measurements were carried out by placing the grid in an empty 1 mm quartz cell (8.0
133 mm \times 1.0 mm \times 36.0 mm (H \times W \times L)) or a 1 mm quartz cell filled with 0.067 M phosphate
134 buffered solution, pH 7.40, or 0.5% (w/v) agarose gel, pH 7.40. In these experiments, the grid is
135 located 1.2 mm above the cover slip of the sensor surface. Additional measurements were carried
136 out where the grid was placed directly on the cover slip of the sensor surface. Measurements
137 were performed at 610 nm with the pixels binned 1×1 and 4×4 using the D100 and the SDI
138 imaging systems. The resolution measured by the grids is given as the maximum number of line
139 pairs per mm (lp/mm) [30] for which the correct number of line pairs can be resolved by eye.

140

141 2.3.4 Resolution measured using lidocaine crystals

142 Lidocaine crystals were arranged in a quartz cuvette and imaged at 254 and 610 nm with pixel
143 binning of 1×1 or 4×4 using the SDI imaging system. The dimensions of the crystals were
144 furthermore measured using a Dino-Lite Premier Digital microscope (AM-7013MZT, AnMo
145 Electronics Corporation, Hsinchu, Taiwan) with a magnification of $\times 50$.

146

147 2.3.5 Density gradients

148 Dissolution of lidocaine from single crystals was investigated in 0.067 M phosphate buffer, pH
149 7.4, and 0.5% w/v agarose gel, pH 7.4, in 1 mm quartz cells (see section 2.3.3) at 254 nm using
150 the SDI imaging system with pixels binned 4×4 . To secure lidocaine single crystals during their
151 dissolution into 0.067 M phosphate buffered solution, pH 7.4, they were fixed at one end with
152 Bantex Tack-all removable adhesive (Bantex A/S, Lynge, Denmark) in the quartz cell.

153

154 2.3.6 Lidocaine diffusion in hydrogel

155 Diffusion of lidocaine from a 0.5% agarose gel at pH 7.4 loaded with 1 mM lidocaine into a
156 blank 0.5% agarose gel, pH 7.4, was studied using the SDI and D100 UV imaging systems in 1
157 mm quartz cells (see section 2.1). The D100 system was applied initially using the standard
158 setting and subsequently with the illumination source, the line end of the round-to-line fibre optic
159 cable, rotated by 90° (cf. section 2.2 for details on the line configuration of the fibre optic
160 bundle). The imaging was performed at a wavelength of 254 nm.

161 The diffusion coefficient (D) of lidocaine in the hydrogel matrix was determined from the UV
162 absorbance maps as a function of time by applying the following derivation of Fick's second law
163 [21,31]:

$$164 \frac{c(x,t)}{c_0} = \frac{1}{2} - \frac{1}{2} \operatorname{erf} \left(\frac{x-x_0}{2\sqrt{t \cdot D}} \right) \quad (1)$$

165 where $C_{(x,t)}$ is the measured concentration as a function of distance and time, C_0 is the initial
166 analyte concentration in the donor gel, erf is the error function, x_0 is the position of the interface
167 between the gel phases and x is the distance from the gel-gel interface and t is the time. Eq. 1 is
168 applicable for one-dimensional diffusion. In Eq. 1, the measured absorbance was used instead of
169 the concentration, because the measured absorbance values were within the linear range
170 according to Lambert Beer's law.

171

172 2.3.7 Diffusion coefficient of lidocaine in phosphate buffered solution

173 The diffusion coefficient of lidocaine in phosphate buffer at pH 7.4 was determined by Taylor
174 dispersion analysis (TDA) at 25 °C as previously described by Ye et al. [32]. A sample of $5.0 \times$
175 10^{-3} M lidocaine in 0.067 M phosphate buffered solution was introduced into a fused silica
176 capillary (75 μm (id) \times 200 μm (od)) by pressure (50 mbar) for 7 s. The sample was forced
177 through the capillary at a constant rate, and the broadening of the lidocaine sample plug due to
178 convective diffusion was detected through two windows in the capillary by UV area imaging at
179 214 nm. The diffusion coefficient of lidocaine was determined from the peak appearance times
180 and the variances of the Gaussian shaped peaks as described by Ye et al. [32].

181

182 **3. Results and discussion**

183 3.1 Performance characteristics of the UV imaging systems

184 The D100 UV imaging system was initially designed for use as detector in separation science
185 [29,33-36]. Subsequently, applications in drug dissolution and release testing have emerged [20].
186 Fig. 1 shows a schematic representation of the basic UV imaging setup for monitoring surface
187 dissolution. The prototype systems have been described in some detail [29,34-36], and
188 methodology for capillary imaging with the D100 is covered elsewhere [28]. The key
189 components include a pulsed Xe lamp emitting light in the wavelength range 190 to 1100 nm,
190 12.5 mm diameter band-pass filters with 10 nm bandwidth (22 nm at 214 nm) for wavelength
191 selection, and a round-to-line fiber optical bundle, where the fibers are arranged in a line
192 configuration at the end, presenting the light to the measurement zone (an array of 90 fibers with
193 a diameter of 100 μm). The light is transmitted through the sample and reaches the detector part
194 consisting of a cover slip, a layer of UV down-converting phosphor and an IBIS4
195 complementary metal oxide semiconductor (CMOS) sensor (Cypress, Mechelen, Belgium) with
196 1280×1024 pixels with dimensions of $7 \mu\text{m} \times 7 \mu\text{m}$ (total imaging area $9 \times 7 \text{ mm}^2$). The CMOS
197 sensor is light sensitive in the range 400 to 1000 nm, thus the role of a UV down-converting
198 phosphor layer ($\text{Gd}_2\text{O}_2\text{S:Tb}$) is to convert light in the UV wavelength range (190 - 290 nm) to
199 the visible wavelength range (a line emission spectrum emitting at several wavelengths with the
200 most prominent emission at 540 nm [37]), where the sensor is sensitive. The principles of UV
201 converting phosphors are described elsewhere [38,39]. The associated electronics and software
202 allow for the construction of images, which may be read in intensity or absorbance mode.

203 The UV imaging systems allow real-time monitoring of the experiments subject to study. Light
204 intensity maps are displayed on a PC using the ActiPix software, and illustrated in Fig. 2 for the
205 D100 and the Sirius SDI. With the D100 (Fig. 2A), the intensity distribution in the xy plane
206 showing a maximum at $y \sim 3 \text{ mm}$ for all x is consistent with the line of fibres positioned above

207 the imager at $y \sim 3$ mm and aligned in the x direction. In the SDI system (Fig. 2B), the light
208 intensity is more uniform across the imaging area, particularly in y direction; however, the light
209 intensity is comparatively lower. The relatively uniform light intensity across the imaging area is
210 related to the incorporation of a collimating lens in the SDI system, leading to a change in how
211 the light is presented to the sample and sensor surface (cf. Fig. 3). The collimating lens
212 constitutes the major difference between the two systems. The presentation of the light to the
213 sample cell and sensor surface is of importance. This is further corroborated by measuring the
214 apparent height from the lower to the upper surface of the flow cell (Fig. 1) to quantify the
215 shadowing effect (Fig. 3). The directly measured height for the open section of this machined
216 part was 3.44 mm. Apparent height values of 4.12 mm and 3.46 mm were reported from the
217 ActiPix software from the images of the cell insert taken with the D100 and the Sirius SDI,
218 respectively. The latter value is in good agreement with the true height, consistent with the light
219 being fairly well collimated. The former value accords with a shadowing effect, in which light at
220 any angle which hits the lower or upper surfaces of the insert is obscured.

221 When using the D100, this may contribute to the difficulties in calculating dissolution rates from
222 UV images and matching those to dissolution rates obtained from the collected effluent, as was
223 the case for paracetamol dissolution studies [20,40]. Also, so called surface concentrations
224 obtained using a D100 UV imaging system should be considered as concentration estimates,
225 since the line of fibres is centred at a y distance greater than the location of the lower surface of
226 the cell insert, the first unobscured ray to reach the imager is transmitted through a layer of fluid
227 significantly elevated from the surface.

228

229 3.1.1 Linearity, noise and LOD

230 UV imaging relies on the molecular absorbance of light. Pixel intensities are converted into
231 absorbance using the instrument software according to:

$$232 \quad A = \log \left(\frac{I_{ref} - I_d}{I_{sig} - I_d} \right) \quad (2)$$

233 where I_d , I_{ref} and I_{sig} are the ADC counts (a measure of intensity which will be referred to as
234 pixel intensity in the following) due to the dark current (electronic noise measured with the lamp
235 turned off), pixel intensity measured with the phosphate buffer (solvent) in the cell (reference
236 signal), and pixel intensity measured during the experiment, respectively. The conversion into
237 absorbance eliminates (to a large extent) the effects of non-uniformity of light intensity across
238 the imaging surface as previously shown [41]. However, imaging artifacts have been observed,
239 mainly in the edges of the images, which are related to low light intensity in this part of the
240 imaging area (this has primarily been observed when using the D100 system). Examples of UV
241 images showing such artifacts can be found in [42,43]. These imaging artifacts are most likely
242 due to drift in the output of the light source over time, which will have the most predominant
243 effect, when the light intensity is low. Drift in light intensity will mainly be an issue in release
244 and diffusion studies, such as described in [42,43], where the self-referencing options of the
245 software used in flow-through type dissolution studies cannot be applied.

246 The absorbance measured by UV imaging may be converted into concentration using Lambert
247 Beer's law by the aid of a calibration curve. Deviations from Lambert Beer's law may occur due
248 to a number of effects: the use of polychromatic rather than monochromatic radiation; the

249 presence of stray light; refractive index changes; close proximity of the absorbing molecules
250 affecting their charge distribution and thereby altering their absorptivity; the molecules taking
251 part in reactions (such as self-association and chemical degradation) and scattering effects due to
252 particles [44-46]. The linearity of the system should therefore be investigated prior to dissolution
253 and release testing experiments. Calibration curves obtained using the SDI imaging system for
254 lidocaine solutions in quartz cells with light paths of 1 and 4 mm, and in a conventional
255 spectrophotometer with a light path of 10 mm are shown in Fig. 4. The use of different
256 instrumentation for absorbance measurements leads to the following apparent molar absorption
257 coefficients (ϵ_{254}) at 254 nm: $6.2 \times 10^2 \text{ M}^{-1} \text{ cm}^{-1}$, $6.5 \times 10^2 \text{ M}^{-1} \text{ cm}^{-1}$, and $4.0 \times 10^2 \text{ M}^{-1} \text{ cm}^{-1}$
258 (RSD < 4%; n = 3), when the light paths were 1 mm (SDI), 4 mm (SDI), and 10 mm (double
259 beam spectrophotometer), respectively. At 214 nm the following apparent molar absorption
260 coefficients (ϵ_{214}) were obtained: $4.7 \times 10^3 \text{ M}^{-1} \text{ cm}^{-1}$, $4.1 \times 10^3 \text{ M}^{-1} \text{ cm}^{-1}$ and $11.2 \times 10^3 \text{ M}^{-1} \text{ cm}^{-1}$
261 (RSD \leq 7%; n = 3), when the light paths were 1, 4, and 10 mm, respectively. The calibration
262 curves were constructed by averaging the absorbance values over a large part of the imaging area
263 from absorbance readings over at least 1 min, in order to minimize the uncertainty and get the
264 best estimate of the molar absorption coefficients. Fig. 4 shows that the calibration curves
265 obtained by UV imaging bend off at absorbance values around 0.5 and 1 at light paths of 1 and 4
266 mm, respectively, while the calibration curve was linear up to an absorbance of approximately 2
267 at a light path of 10 mm using the conventional spectrophotometer. We have previously reported
268 a ϵ_{254} of $4.36 \times 10^2 \text{ M}^{-1} \text{ cm}^{-1}$ for lidocaine in the same phosphate buffer using a 3 mm light path
269 quartz cell and an SDI300 imaging system (using a D100 sensor head configuration) [16]. The
270 results show the importance of using a calibration curve that is constructed in the quartz cell, and
271 using the band pass filter as well as the same system as the actual measurements will be

272 performed on. The performance of the total system is dependent on the light path, collimation of
273 light and band pass width as well as the performance of the detector.

274 During the absorbance measurements of the standard solutions for construction of the calibration
275 curves, the noise of the SDI imaging system was assessed. The peak to peak noise was estimated
276 to be ~18 and ~35 mAU at 214 and 254 nm, respectively (Supplementary data Fig. S2; quartz
277 cell with 4 mm light path). A higher light intensity at 214 nm is the reason for the lower noise
278 level at 214 nm as compared to 254 nm. From the data shown in Supplementary data Fig. S2 and
279 the slope of the calibration curve, the LOD ($S/N = 3$) for lidocaine in phosphate buffer was
280 calculated to 3.3×10^{-5} M and 4.0×10^{-4} M at 214 and 254 nm, respectively. These LOD values
281 are based on readings with individual effective pixels (10×1 binning), which together with the
282 low molar absorption coefficients provide the reason for the relatively high LODs.

283 Fig. 5 shows detector response (pixel intensity) as a function of wavelength for the band-pass
284 filters available in our lab using the SDI imaging instrument. The pixel intensities were read
285 from the same area (5.60×4.76 mm²) in all experiments to limit effects of the non-uniform
286 intensity across the image surface. The detector response depends on the lamp intensity,
287 transmittance of the band-pass filters, and efficiency of the UV down-converting phosphor in the
288 UV range, and how these parameters vary as a function of the wavelength. Fig. 5 reveals a low
289 pixel intensity/detector response in the wavelength interval 300 - 350 nm making UV imaging
290 difficult in this range. The relatively poor performance in the range 300 - 350 nm results from the
291 combination of a relatively low light output from the Xe lamp and poor efficiency of the UV
292 down-converting phosphor ($Gd_2O_2S:Tb$ [37]). These issues have also been described for a CCD
293 detector utilizing UV down-converting phosphors [38,39]. Fig. 5 highlights another interesting

294 feature requiring attention in, namely that the transmission efficiency of the individual band pass
295 filters vary.

296

297 3.1.2 Resolution of the UV imaging systems

298 Previous studies in our lab have indicated that the resolution of the UV imaging system is
299 different in the horizontal (x) and vertical (y) direction. In the following, studies were performed
300 to shed light on the resolution of the UV imaging systems. The resolution was assessed using
301 grids with line pairs (a black and transparent line constitute a line pair) having widths between 10
302 and 400 μm . The line pair-width intervals were 10 μm below 100 μm , and 20 μm above 100 μm .
303 The measurements were performed in the visible wavelength range, where the film is transparent
304 and the grid lines absorb the light. Fig. 6 shows the absorbance maps of a grid with a line width
305 of 100 μm placed on the cover slip of the sensor surface or in a quartz cell, leading to a position
306 of the grid 1.2 mm above the cover slip of the sensor surface for the D100 and SDI imaging
307 system due to the thickness of the quartz wall. High and low absorbance values are indicated by
308 red and blue coloring, respectively, in the absorbance maps. A clear difference in the
309 performance of the imaging systems in the x- and y-direction is seen from these images. This is
310 due to the light coming from the fiber optic bundle with a line configuration above the CMOS
311 chip (Fig. 3). An improved resolution is observed when the grid-lines are placed parallel to the
312 light source line. In Table 1, the estimated resolution of the imaging systems is given as
313 maximum line pairs per mm (lp/mm). In empty quartz cells and quartz cells filled with phosphate
314 buffered solution or 0.5% (w/v) agarose hydrogel at pH 7.4, the resolution of the D100 and SDI
315 imaging systems with pixels binned 4×4 (nominal resolution of 28 μm) were determined to be

316 1.7 and 2.5 lp/mm, respectively, in the x-direction and 10 and 12.5 lp/mm, respectively, in the y-
317 direction. A resolution of 12.5 lp/mm indicates that the system is able to separate and measure
318 lines with a width of 40 μm . According to Table 1, the resolution is substantially better when the
319 grid is placed directly on the cover slip of the sensor surface as compared to on the quartz cell.
320 Thus, the resolution depends on the position of the object above the cover slip of the sensor
321 surface, and it decreases as the object gets closer to the light emission slit. This can be seen as a
322 result of a shadowing / optical lever effect (Fig. 3 and section 3.1). The pixel-binning (1×1
323 versus 4×4) does not seem to have a large effect on the resolution. The results show that the
324 minimum resolvable feature size is greater than the size of the effective pixel. This is primarily
325 due to the optical lever effect combining the width of the light source (100 μm diameter for the
326 optical fibres) and the relatively short (9 mm) distance from fibre output to sensor surface. By
327 comparison with the D100, Table 1 highlights an improved resolution for the SDI due to
328 movement of the source to a greater distance away from the sensor surface and incorporation of a
329 collimating lens. The highest resolution was observed using the SDI system without any pixel
330 binning, when the grid was placed on the cover slip of the sensor surface, and was measured to
331 be 12.5 and 16.7 lp/mm (corresponding to line widths of 40 and 30 μm) in the x- and y-direction,
332 respectively.

333 Since the grids were not transparent in the UV range, and because the resolution also depends on
334 the level of contrast available, an alternative approach was developed to estimate resolution in
335 this spectral region which is of primary interest for dissolution studies. The dissolution of
336 lidocaine from selected single crystals into stagnant phosphate buffered solution has earlier been
337 investigated by UV imaging at 254 nm [16]. In order to show how the spatial resolution of the
338 two imaging systems influences the size and shape of the imaged objects, such lidocaine crystals

339 were imaged at wavelengths of 254 and 610 nm in the absence of dissolution medium.
340 Microscope photographs and UV images of selected lidocaine crystals are shown in Fig. 7A and
341 B. Both Fig. 6 and 7 show that the resolution of the imaging systems is better in the y-direction
342 as compared to in the x-direction. In the current project, the width of the lidocaine crystal was
343 measured at a selected position under the microscope to be 185.6 μm (Fig. 7A). The UV-Vis
344 systems were able to identify and detect lidocaine crystals, but the width of the crystal placed
345 parallel or perpendicular to the emission slit was measured to 230 or 480 μm , respectively, by
346 the SDI system with pixels binned 4 x 4 at 254 nm (Figs. 7B and C). It is evident that UV-Vis
347 imaging overestimates the thickness of the lidocaine crystal; this is due to the optical lever and
348 shadowing effects with the object (Fig. 7B).

349 Absorbance - distance profiles were constructed from the absorbance maps of the lidocaine
350 crystals, and the resolution of the imaging system was determined based on the sharpness of the
351 interface, as previously described by Chan et al. [47], by measuring the distance over which the
352 normalized absorbance fell from 95 to 5 % of the maximum value. The normalized absorbance -
353 distance profiles of the selected lidocaine crystals are shown in Fig. 7D. Based on this procedure,
354 the resolution of the SDI imaging system at 254 nm with the pixels binned 4 \times 4 was estimated
355 to be 250 and 75 μm in the x- and y-directions, respectively. Table 2 shows the estimated
356 resolution from the crystals by the SDI system with pixels binned 1 \times 1 and 4 \times 4 at 254 and 610
357 nm. Overall, these data indicate that pixel binning is not the limiting factor when it comes to
358 resolution; the dimension of the light emitting slit and shadowing effects seem to be significant
359 contributing factors.

360

361 3.2 Effects of hydrogels on density effects

362 The dissolution behavior of lidocaine from selected single crystals into stagnant phosphate buffer
363 has previously been investigated by UV imaging. The study showed that the dissolved lidocaine
364 seems to gather at the bottom of the quartz cell, which may be explained by the formation of a
365 density gradient as lidocaine dissolves leading to natural convection [16]. Hydrogel matrixes
366 have been shown to suppress natural convection due to density gradients [43,48-50]. In the
367 current study, the effect of introducing a 0.5% (w/v) agarose hydrogel at pH 7.4 as a dissolution
368 medium on the dissolution behavior of a single lidocaine crystal under stagnant conditions was
369 visualized. Fig. 8 shows the absorbance maps of the dissolution behavior of lidocaine. The image
370 resolution is not affected by introduction of the gel (Fig. 8), which is understandable in the light
371 of the discussion in section 3.1, and the crystals are still readily apparent. During dissolution of
372 lidocaine in the hydrogel matrix, the absorbance contours mapped around the crystals were
373 almost symmetrical (Fig. 8A). This contrasts with the irregular contours around the crystals in
374 the phosphate buffered solution (Fig. 8B). The symmetrical absorbance maps formed in the
375 hydrogel matrix indicate that the natural convection seen in aqueous solution has been
376 effectively suppressed in the hydrogel matrix. The mass transport of dissolved lidocaine in the
377 hydrogel is solely due to diffusion whereas transport of dissolved lidocaine the solution is due to
378 convective currents as well as diffusion.

379

380 3.3 Lidocaine diffusion in hydrogel

381 Diffusion coefficients of drug compounds in hydrogel matrixes have previously been determined
382 by fitting data to equations based on Fick's second law [21,42]. In these studies, the samples are
383 placed in a manner such that the diffusion can be assumed to occur only in the x-direction. The
384 determined diffusion coefficients are influenced by the defined position of the interface, x_0 (cf.
385 Eq. 1), and the precision with which the position of the interface can be determined may
386 therefore be important for the results obtained. In our previous diffusion studies using a D100
387 imaging system [21,42], the interface between the sample and the release (acceptor) medium was
388 perpendicular to the fibre optic line source, i.e. oriented such that diffusion occur in x-direction
389 where the imaging system has the lowest resolution. The results in section 3.1.2 showed that the
390 orientation of the objects relative to the line light source has a significant impact on the
391 resolution. Tests were therefore undertaken to check whether rotation of the output end of the
392 round-to-line fibre optic cable by 90° influenced the initial appearance and sharpness of the
393 interface between a hydrogel loaded with lidocaine and a blank hydrogel. Interestingly, no
394 difference in the sharpness of the boundary between the hydrogels was observed (data not
395 shown), and the slopes of the tangent to the curves at the interface were similar at time zero.
396 However, the curves were associated with more scatter when the line source was rotated 90° ,
397 which may be attributed to the higher resolution in this direction. By applying Eq. 1 to the
398 normalized absorbance-distance profiles (Fig. 9A), diffusion coefficients of lidocaine in the
399 hydrogel matrixes were determined. The apparent diffusion coefficients were found to decrease
400 with time (10 - 180 min). By plotting the diffusion coefficient as a function of the reciprocal of
401 time (Fig. 9B), the apparent diffusion coefficient was obtained from the intercept of the straight
402 line with the y-axis [21,51]. The diffusion coefficient was determined to be $(6.3 \pm 0.05) \times 10^{-10}$
403 m^2/s , $(6.9 \pm 0.05) \times 10^{-10} \text{ m}^2/\text{s}$ and $(7.5 \pm 0.11) \times 10^{-10} \text{ m}^2/\text{s}$ ($n = 3 \times 3$) at $22.0 \pm 1.0 \text{ }^\circ\text{C}$ using

404 the D100, SDI and D100 system with the line rotated 90°, respectively. Brouneus and co-
405 workers have determined the diffusion coefficient of lidocaine hydrochloride to be (7.49 ± 0.43)
406 $\times 10^{-10} \text{ m}^2/\text{s}$ ($n = 8$) in 1% (w/w) agarose gel at 25 °C by measuring the amount of lidocaine
407 diffusing from a well stirred solution of 25 mM lidocaine into the gel at specified time points
408 [52]. The diffusion coefficient of lidocaine in phosphate buffered solution was determined to be
409 $(5.8 \pm 0.2) \times 10^{-10} \text{ m}^2/\text{s}$ using TDA, which is in accordance with the previously determined
410 diffusion coefficient of lidocaine in buffer solution at pH 7.4 ($(5.5 \pm 0.2) \times 10^{-10} \text{ m}^2/\text{s}$) [32]. Due
411 to the unhindered diffusion of small molecules in the agarose hydrogel matrix, the diffusion
412 coefficient of lidocaine obtained in the hydrogel was expected to be comparable to the value
413 obtained in aqueous solution. The observed variation in the obtained diffusion coefficients for
414 lidocaine in agarose gels and in solution is within the normal range, when different methods are
415 applied. Using the current UV imaging instrumentation, where the effective height in the y-
416 direction is 3.9 mm and the length in the x-direction is ~ 8 mm for the setup used for the
417 diffusion experiments, it is advantageous to study diffusion in the x-direction due to a longer
418 potential diffusion distance allowing the process to be followed for longer periods of time. The
419 effective imaging area in the x-direction is 7 - 9 mm in the D100 and SDI system, while it is 4 - 6
420 mm in the D100 system with the line of fibres rotated 90° and the fall of intensity with distance
421 as noted in Fig. 2A. The reason why a difference with respect to sharpness of the interface was
422 not observed using the different UV imaging setups may be due to the immediate diffusion of
423 lidocaine as the lidocaine loaded gel is placed side by side with the blank hydrogel matrix. The
424 time for the quartz cell containing the sample to be placed under the UV imaging sensor head
425 varies between experiments and is generally in the order of 1 to 5 min. The root-mean-square
426 distances ($\langle x^2 \rangle^{1/2}$) of lidocaine at 1 and 5 min were calculated to be 300 and 670 μm ,

427 respectively, using the formula for one-dimensional diffusion $\langle x^2 \rangle^{1/2} = \sqrt{2 \times D \times t}$ and a
428 diffusion coefficient of $7.5 \times 10^{-10} \text{ m}^2/\text{s}$. These are relatively large distances, in comparison to the
429 resolution which is in the order of 20 to 200 μm . Thus, the experimental procedure rather than
430 instrument performance appears to be the limiting factor in these diffusion assays.

431

432 **4. Conclusion**

433 The present study showed that the apparent absorption coefficients depend on the spectroscopic
434 instrumentation used, highlighting the importance of investigating the linearity prior to
435 dissolution imaging. For quantitative results, the apparent molar absorption coefficient should be
436 determined using the UV imaging system rather than a conventional spectrophotometer.

437 The main difference between the D100 and SDI imaging systems is the introduction of a
438 collimating lens in the latter system. This leads to several improvements in instrument
439 performance. The SDI imaging system showed an increased uniformity of the light intensity
440 across the imaging area as well as an improved resolution, which may be explained by a reduced
441 shadowing effect. Both systems have as light source a line of 100 μm fibres aligned in the x-
442 direction, which means that resolution is greatest in the y-direction. The main parameter
443 influencing the resolution was found to be the distance of the object above the cover slip and the
444 sensor surface, consistent with the optical lever effect. Under the most favorable conditions,
445 with a grid placed directly on the cover slip, the resolution was estimated to 12.5 and 16.7 lp/mm
446 in the x- and y-directions, respectively. Effects related to positioning of objects should therefore
447 be taken into account during designing of experiments and image interpretation.

448 UV imaging offers detailed insights into dissolution processes as shown for lidocaine crystals. In
449 aqueous solution, natural convection leads to dense lidocaine solution accumulating at the
450 bottom of the cell. Agarose gels are shown to be able to suppress the effect of natural convection
451 arising from density gradients, in accordance with previous studies [16]. Hydrogels may thus be
452 suitable matrixes for visualizing and characterizing dissolution (and release) processes under
453 stagnant conditions. In relation to studying diffusion processes in hydrogels, the positioning of
454 the diffusion boundary relative to the fibre optic line source (parallel versus perpendicular) did
455 not improve the sharpness of the interface even at the shortest measurement time. Calculations
456 of root-mean-square distances for diffusion showed that this could have been due to diffusion
457 occurring as the experiment was being setup, rather than the instrument limiting the sharpness of
458 the diffusion boundary.

459 The knowledge obtained in the current study about the instrument performance characteristics
460 will be helpful in the design and interpretation of UV imaging based release and dissolution
461 studies.

462

463 **Acknowledgements**

464 This project has received funding from the European Union's Horizon 2020 research and
465 innovation program under the Marie Skłodowska-Curie grant agreement No 644056. The authors
466 alone are responsible for the content and writing of this paper.

467

468 **References**

- 469 [1] J. Emami, In vitro - in vivo correlation: from theory to applications, *J. Pharm. Pharmac. Sci.*
470 9 (2006) 169-189.
- 471 [2] M. Windbergs, D.A. Weitz, Drug dissolution chip (DDC): A microfluidic approach for drug
472 release. *Small* 7 (2011) 3011-3015.
- 473 [3] M. Kuentz, Analytical technologies for real-time drug dissolution and precipitation testing
474 on a small scale, *J. Pharm. Pharmacol.* 67 (2014) 143-159.
- 475 [4] A.V. Ewing, G.S. Clarke, S.G. Kazarian, Attenuated total reflection-Fourier transformed
476 infrared spectroscopic imaging of pharmaceuticals in microfluidic devices, *Biomicrofluidics*
477 10 (2016) 024125.
- 478 [5] K. Mäder, G. Bacic, A. Domb, O. Elmalak, R. Langer, H.M. Swartz, Noninvasive in vivo
479 monitoring of drug release and polymer erosion from biodegradable polymers by EPR
480 spectroscopy and NMR imaging, *J. Pharm. Sci.* 86 (1997) 126-134.
- 481 [6] J.C. Richardson, R.W. Bowtell, K. Mäder, C.D. Melia, Pharmaceutical applications of
482 magnetic resonance imaging (MRI), *Adv. Drug Deliv. Rev.* 57 (2005) 1191-1209.
- 483 [7] K.P. Nott, Magnetic resonance imaging of tablet dissolution, *Eur. J. Pharm. Biopharm.* 74
484 (2010) 78-83.
- 485 [8] C. Chen, L.F. Gladden, M.D. Mantle, Direct visualization of in vitro drug mobilization from
486 lescol XL tablets using two-dimensional ¹⁹F and ¹H magnetic resonance imaging, *Mol.*
487 *Pharm.* 11 (2013) 630-637.
- 488 [9] S.G. Kazarian, J. van der Weerd, Simultaneous FTIR spectroscopic imaging and visible
489 photography to monitor tablet dissolution and drug release, *Pharm. Res.* 25 (2008) 853-860.
- 490 [10] J.A. Kimber, S.G. Kazarian, F. Stepanek, Microstructure-based mathematical modelling and
491 spectroscopic imaging of tablet dissolution, *Comput. Chem. Eng.* 35 (2011) 1328-1339.
- 492 [11] S.G. Kazarian, A.V. Ewing, Applications of Fourier transform infrared spectroscopic
493 imaging to tablet dissolution and drug release, *Expert Opin. Drug Deliv.* 10 (2013) 1207-
494 1221.
- 495 [12] M. Windbergs, M. Jurna, H.L. Offerhaus, J.L. Herek, P. Kleinebudde, C.J. Strachan,
496 Chemical imaging of oral solid dosage forms and changes upon dissolution using coherent
497 anti-stokes Raman scattering microscopy, *Anal. Chem.* 81 (2009) 2085-2091.
- 498 [13] G.S. Bajwa, K. Hoebler, C. Sammon, P. Timmins, C.D. Melia, Microstructural imaging of
499 early gel layer formation in HPMC matrices, *J. Pharm. Sci.* 95 (2006) 2145-2157.

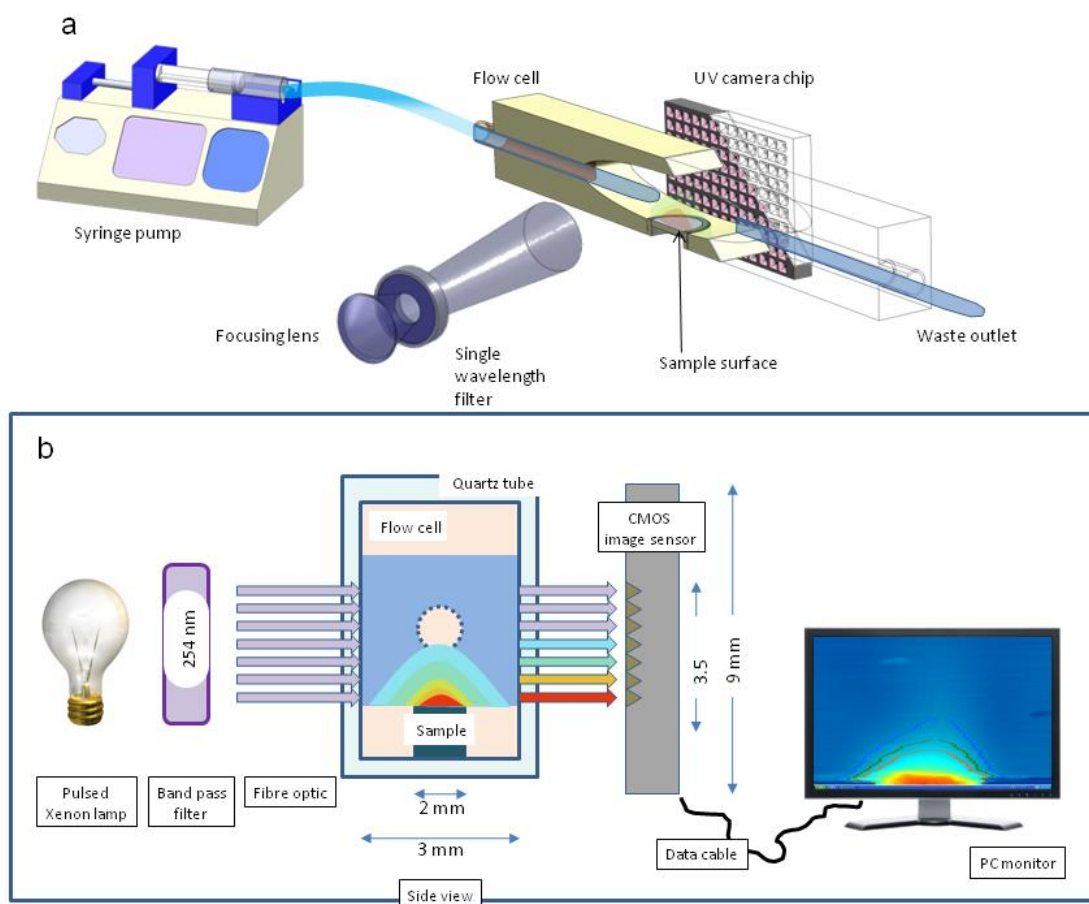
- 500 [14] F. Brandl, F. Kastner, R.M. Gschwind, T. Blunk, J. Tessmar, A. Göpferich, Hydrogel-based
501 drug delivery systems: Comparison of drug diffusivity and release kinetics, *J. Control.*
502 *Release* 142 (2010) 221-228.
- 503 [15] J.P. Boetker, M. Savolainen, V. Koradia, F. Tian, T. Rades, A. Müllertz, C. Cornett, J.
504 Rantanen, J. Østergaard, Insights into the early dissolution events of amlodipine using UV
505 imaging and Raman spectroscopy, *Mol. Pharm.* 8 (2011) 1372-1380.
- 506 [16] J. Østergaard, F. Ye, J. Rantanen, A. Yaghmur, S.W. Larsen, C. Larsen, H. Jensen,
507 Monitoring lidocaine single-crystal dissolution by ultraviolet imaging, *J. Pharm. Sci.* 100
508 (2011) 3405-3410.
- 509 [17] W.L. Hulse, J. Gray, R.T. Forbes, A discriminatory intrinsic dissolution study using UV area
510 imaging analysis to gain additional insights into the dissolution behaviour of active
511 pharmaceutical ingredients, *Int. J. Pharm.* 434 (2012) 133-139.
- 512 [18] M. Li, N. Qiao, K. Wang, Influence of sodium lauryl sulfate and tween 80 on carbamazepine-
513 nicotinamide cocrystal solubility and dissolution behaviour, *Pharmaceutics* 5 (2013) 508-
514 524.
- 515 [19] N. Qiao, K. Wang, W. Schlindwein, A. Davies, M. Li, In situ monitoring of carbamazepine-
516 nicotinamide cocrystal intrinsic dissolution behaviour, *Eur. J. Pharm. Biopharm.* 83 (2013)
517 415-426.
- 518 [20] J. Østergaard, J. Lenke, S.S. Jensen, Y. Sun, Y. Fengbin, UV imaging for in vitro dissolution
519 and release studies: Initial experiences, *Dissolut. Technol.* 22 (2014) 27-38.
- 520 [21] F. Ye, A. Yaghmur, H. Jensen, S.W. Larsen, C. Larsen, J. Østergaard, Real-time UV imaging
521 of drug diffusion and release from Pluronic F127 hydrogels, *Eur. J. Pharm. Sci.* 43 (2011)
522 236-243.
- 523 [22] J. Østergaard, E. Meng-Lund, S.W. Larsen, C. Larsen, K. Petersson, J. Lenke, H. Jensen,
524 Real-time UV imaging of nicotine release from transdermal patch, *Pharm. Res.* 27 (2010)
525 2614-2623.
- 526 [23] J. Østergaard, J.X. Wu, K. Naelapaa, J.P. Boetker, H. Jensen, J. Rantanen, Simultaneous UV
527 imaging and raman spectroscopy for the measurement of solvent-mediated phase
528 transformations during dissolution testing, *J. Pharm. Sci.* 103 (2014) 1149-1156.
- 529 [24] F. Ye, S.W. Larsen, A. Yaghmur, H. Jensen, C. Larsen, J. Østergaard, Drug release into
530 hydrogel-based subcutaneous surrogates studied by UV imaging, *J. Pharm. Biomed. Anal.*
531 71 (2012) 27-34.
- 532 [25] Y. Lu, L. Mingzhong, Simultaneous rapid determination of the solubility and diffusion
533 coefficients of poorly water-soluble drug based on a novel UV imaging system, *J. Pharm.*
534 *Sci.* 105 (2016) 131-138.

- 535 [26] N. Gautschi, P.V. Hoogevest, M. Kuentz, Amorphous drug dispersions with mono- and
536 diacyl lecithin: On molecular categorization of their feasibility and UV dissolution imaging,
537 Int. J. Pharm. 491 (2015) 218-230.
- 538 [27] S.S. Jensen, H. Jensen, E.H. Møller, C. Cornett, F. Siepman, J. Siepman, In vitro release
539 studies of insulin from lipid implants in solution and in a hydrogel matrix mimicking the
540 subcutis, Eur. J. Pharm. Sci. 81 (2016) 103-112.
- 541 [28] F. Oukacine, L. Garrelly, B. Romestand, D.M. Goodall, T. Zou, H. Cottet, Focusing and
542 mobilization of bacteria in capillary electrophoresis, Anal. Chem. 83 (2011) 1571-1578.
- 543 [29] P.L. Urban, D.M. Goodall, E.T. Bergström, N.C. Bruce, Electrophoretically mediated
544 microanalysis of a nicotinamide adenine dinucleotide-dependent enzyme and its facile
545 multiplexing using an active pixel sensor UV detector, J. Chromatogr. A 1162 (2007) 132-
546 140.
- 547 [30] ISO 12233:2014(en) Photography - Electronic still picture imaging - Resolution and spatial
548 frequency responses. International Organization for Standardization, Geneva, Switzerland.
549 <https://www.iso.org/obp/ui/#iso:std:iso:12233:ed-2:v1:en>. 2015 (Accessed 25-06-2015).
550
- 551 [31] J. Crank The mathematics of diffusion, Oxford University Press, Oxford, 1975.
- 552 [32] F. Ye, H. Jensen, S.W. Larsen, A. Yagmur, C. Larsen, J. Østergaard, Measurement of drug
553 diffusivities in pharmaceutical solvents using Taylor dispersion analysis, J. Pharm. Biomed.
554 Anal. 61 (2011) 176-183.
- 555 [33] M. Kulp, P.L. Urban, M. Kaljurand, E.T. Bergström, D.M. Goodall, Visualization of
556 electrophoretically mediated in-capillary reactions using a complementary metal oxide
557 semiconductor-based absorbance detector, Anal. Chim. Acta 570 (2006) 1-7.
- 558 [34] P.L. Urban, D.M. Goodall, E.T. Bergstrom, N.C. Bruce, Electrophoretic assay for
559 penicillinase: Substrate specificity screening by parallel CE with an active pixel sensor,
560 Electrophoresis 28 (2007) 1926-1936.
- 561 [35] P.L. Urban, D.M. Goodall, A.Z. Carvalho, E.T. Bergström, A. Van Schepdael, N.C. Bruce,
562 Multi-compound electrophoretic assays for tyramine oxidase with a UV area detector
563 imaging multiple windows on a looped capillary, J. Chromatogr. A 1206 (2008) 52-63.
- 564 [36] J. Østergaard, H. Jensen, Simultaneous evaluation of ligand binding properties and protein
565 size by electrophoresis and Taylor dispersion in capillaries, Anal. Chem. 81 (2009) 8644-
566 8648.
- 567 [37] S. Chatterjee, V. Shanker, P.K. Ghosh, Trapping parameters and kinetics in Gd₂O₂S:Tb
568 phosphor, Solid state Commun. 80 (1991) 877-880.
- 569 [38] M.M. Blouke, M.W. Cowens, J.E. Hall, J.A. Westphal, A.B. Christensen, Ultraviolet
570 downconverting phosphor for use with silicon CCD imagers, Appl. Opt. 19 (1980) 3318-
571 3321.

- 572 [39] M.W. Cowens, M.M. Blouke, T. Fairchild, J.A. Westphal, Coronene and liumogen as VUV
573 sensitive coatings for Si CCD imagers: a comparison, *Appl. Opt.* 19 (1980) 3727-3728.
- 574 [40] J.P. Boetker, J. Rantanen, T. Rades, A. Müllertz, J. Østergaard, H. Jensen, A new approach
575 to dissolution testing by UV imaging and finite element simulations, *Pharm. Res.* 30 (2013)
576 1328-1337.
- 577 [41] J. Østergaard, E. Meng-Lund, S. Larsen, C. Larsen, K. Petersson, J. Lenke, H. Jensen, Real-
578 Time UV imaging of nicotine release from transdermal patch, *Pharm. Res.* 27 (2010) 2614-
579 2623.
- 580 [42] S.S. Jensen, H. Jensen, C. Cornett, E.H. Møller, J. Østergaard, Insulin diffusion and self-
581 association characterized by real-time UV imaging and Taylor dispersion analysis, *J. Pharm.*
582 *Biomed. Anal.* 92 (2014) 203-210.
- 583 [43] M.H. Gaunø, T. Vilhelmsen, C.C. Larsen, J.P. Boetker, J. Wittendorff, J. Rantanen, J.
584 Østergaard, Real-time in vitro dissolution of 5-aminosalicylic acid from single ethyl
585 cellulose coated extrudates studied by UV imaging, *J. Pharm. Biomed. Anal.* 83 (2013) 49-
586 56.
- 587 [44] S. Görög *Ultraviolet-visible spectrophotometry in pharmaceutical analysis*, CRC Press,
588 Boca Raton, 1995.
- 589 [45] L. Sommer *Analytical absorption spectrophotometry in the visible and ultraviolet: The*
590 *principles*, Elsevier Science Publishers, Amsterdam, 1989.
- 591 [46] D.S. Hage, J.D. Carr *Analytical chemistry and quantitative analysis*, Prentice Hall, Boston,
592 2011.
- 593 [47] K.L. Chan, S.G. Kazarian, New opportunities in micro- and macro-attenuated total reflection
594 infrared spectroscopic imaging: spatial resolution and sampling versatility, *Appl. Spectrosc.*
595 57 (2003) 381-389.
- 596 [48] S.S. Jensen, H. Jensen, C. Cornett, E.H. Møller, J. Østergaard, Real-time UV imaging
597 identifies the role of pH in insulin dissolution behavior in hydrogel-based subcutaneous
598 tissue surrogate, *Eur. J. Pharm. Sci.* 69 (2015) 26-36.
- 599 [49] B. Lorber, C. Sauter, A. Theobald-Dietrich, A. Moreno, P. Schellenberger, M.C. Robert, B.
600 Capelle, S. Sanglier, N. Potier, R. Giege, Crystal growth of proteins, nucleic acids, and
601 viruses in gels, *Prog. Biophys. Mol. Biol.* 101 (2009) 13-25.
- 602 [50] J.M. Garcia-Ruiz, M.L. Novella, R. Moreno, J.A. Gavira, Agarose as crystallization media
603 for proteins I: transport processes, *J. Cryst. Growth* 232 (2001) 165-172.
- 604 [51] V.F. Felicetta, A.E. Markham, Q.P. Peniston, J.L. McCarthy, A study of diffusion in agar
605 gels by a light absorption method, *J. Am. Chem. Soc.* 71 (1949) 2879-2885.

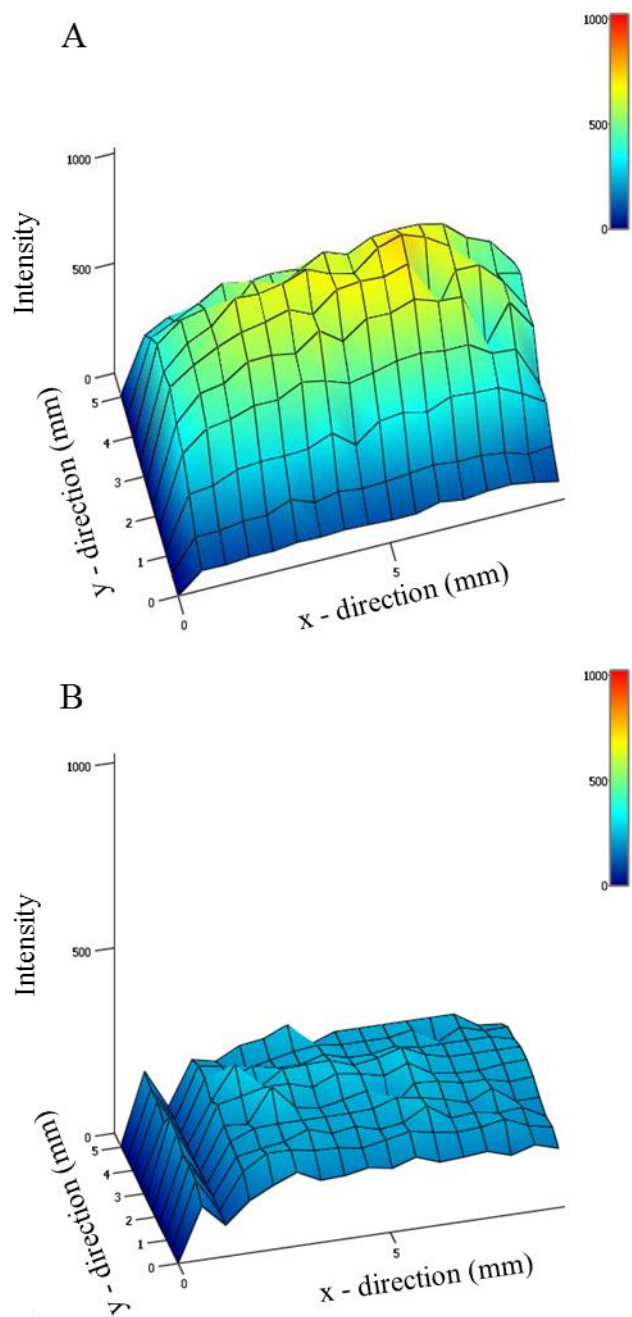
606 [52] F. Brouneus, K. Karami, P. Beronius, L.O. Sundelöf, Diffusive transport properties of some
607 local anesthetics applicable for iontophoretic formulation of the drugs, *Int. J. Pharm.* 218
608 (2001) 57-62.

609 **Figures:**



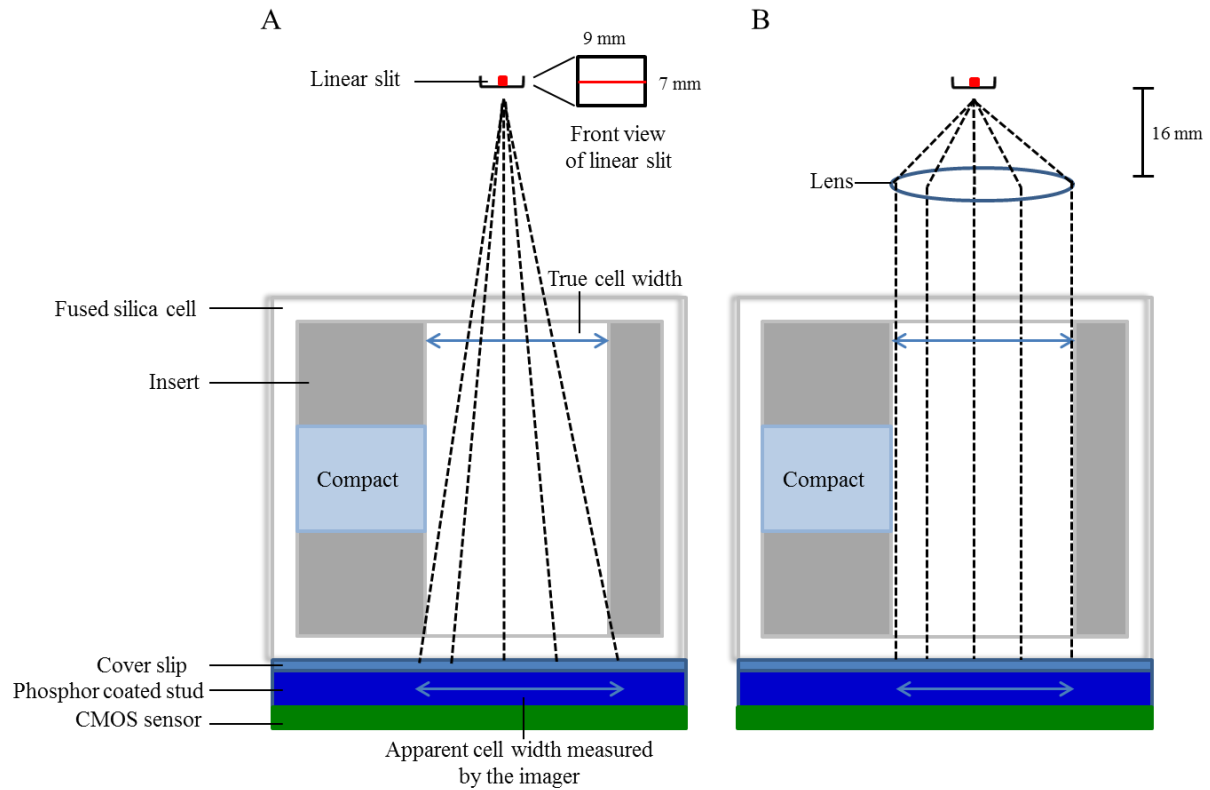
610

611 **Fig. 1.** Schematic representation of the UV imaging setup (reprinted from [22] with permission
612 from Springer).



613

614 **Fig. 2.** Light intensity maps of the imaging area in the x- and y-direction of the A) ActiPix D100
 615 UV area imaging system (Paraytec Ltd, York, UK) and B) Sirius SDI (Sirius Analytical Ltd, East
 616 Sussex, UK) imaging system with pixels binned 1×1 at 254 nm.

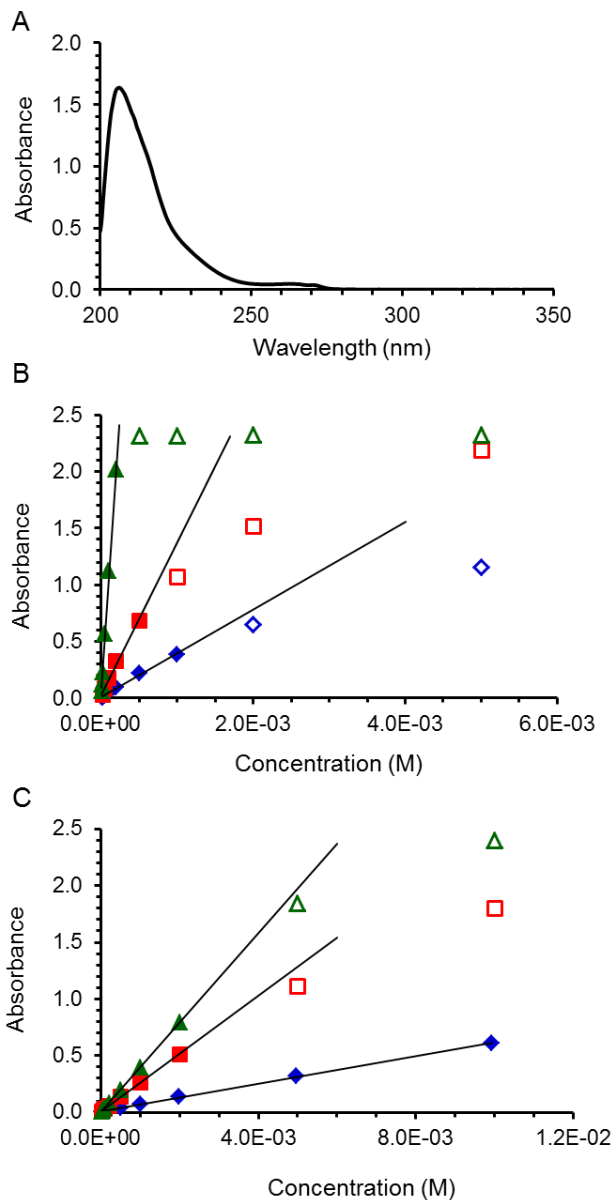


617

618 **Fig. 3.** Schematic illustration of sensor head components and light paths for the D100 (A) and

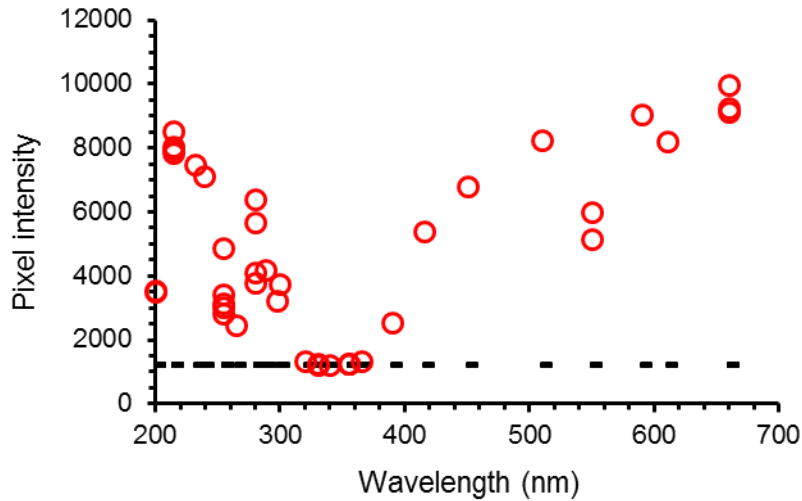
619 SDI (B) imaging systems. The drawings are not to scale, and the linear slit height is 16 mm

620 above the cylinder lens. Note the change in sensor head orientation relative to Fig. 1.




621

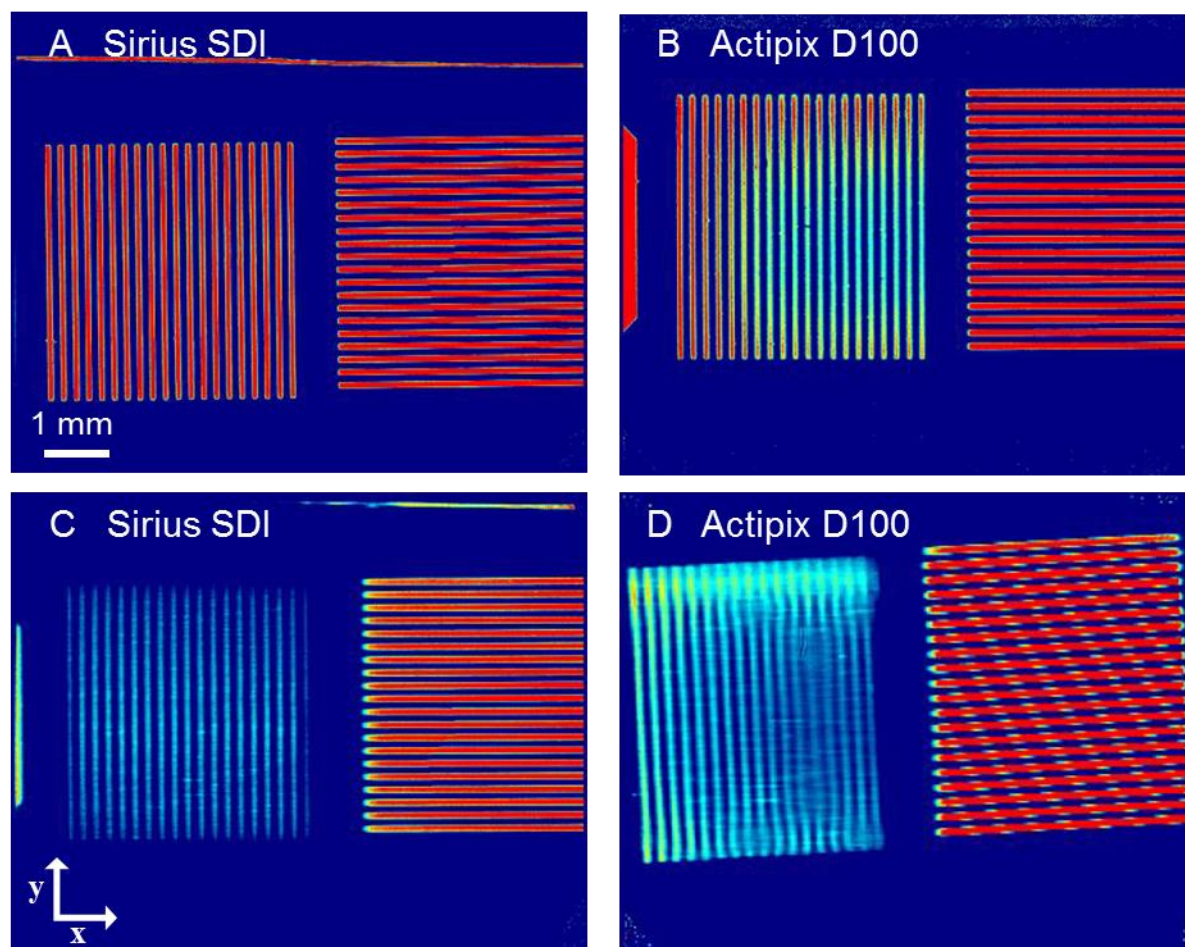
622 **Fig. 4.** A) UV scan of 1.0×10^{-4} M lidocaine in 0.067 M phosphate buffered solution, pH 7.4,
 623 obtained using a conventional spectrophotometer. Calibration curves of lidocaine in phosphate
 624 buffered solution at pH 7.4 obtained in quartz cells with a light path of 1 (◆, ◇) and 4 mm (■, □)
 625 using the SDI UV imaging and 10 mm (▲, △) by a conventional spectrophotometer at B) 214
 626 and C) 254 nm. The lines are the linear regression using only the closed symbols, and the open
 627 symbols represent the points that are deviating from linearity.



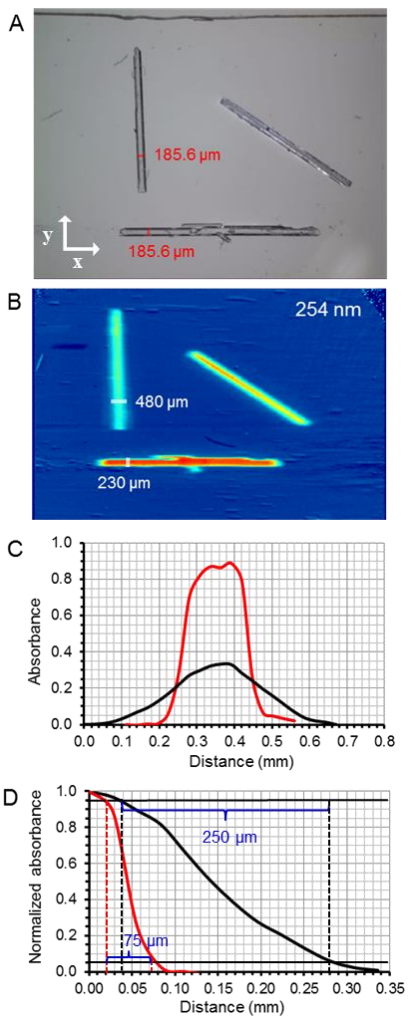
628

629 **Fig. 5.** Pixel intensities as a function of wavelength for the interference band-pass filters using the
 630 SDI UV imaging instrument (\circ), and the measured intensities (the dark current), when the lamp
 631 was turned off ($-$). The pixel intensities plotted were average values read from a selected image
 632 area ($5.60 \times 4.76 \text{ mm}^2$). At some wavelengths, the pixel intensity was measured by several filters,
 633 some of which had different transmission efficiency. All filters were measured on the same system
 634 in a single experimental session.

Orientation of emission slit: 

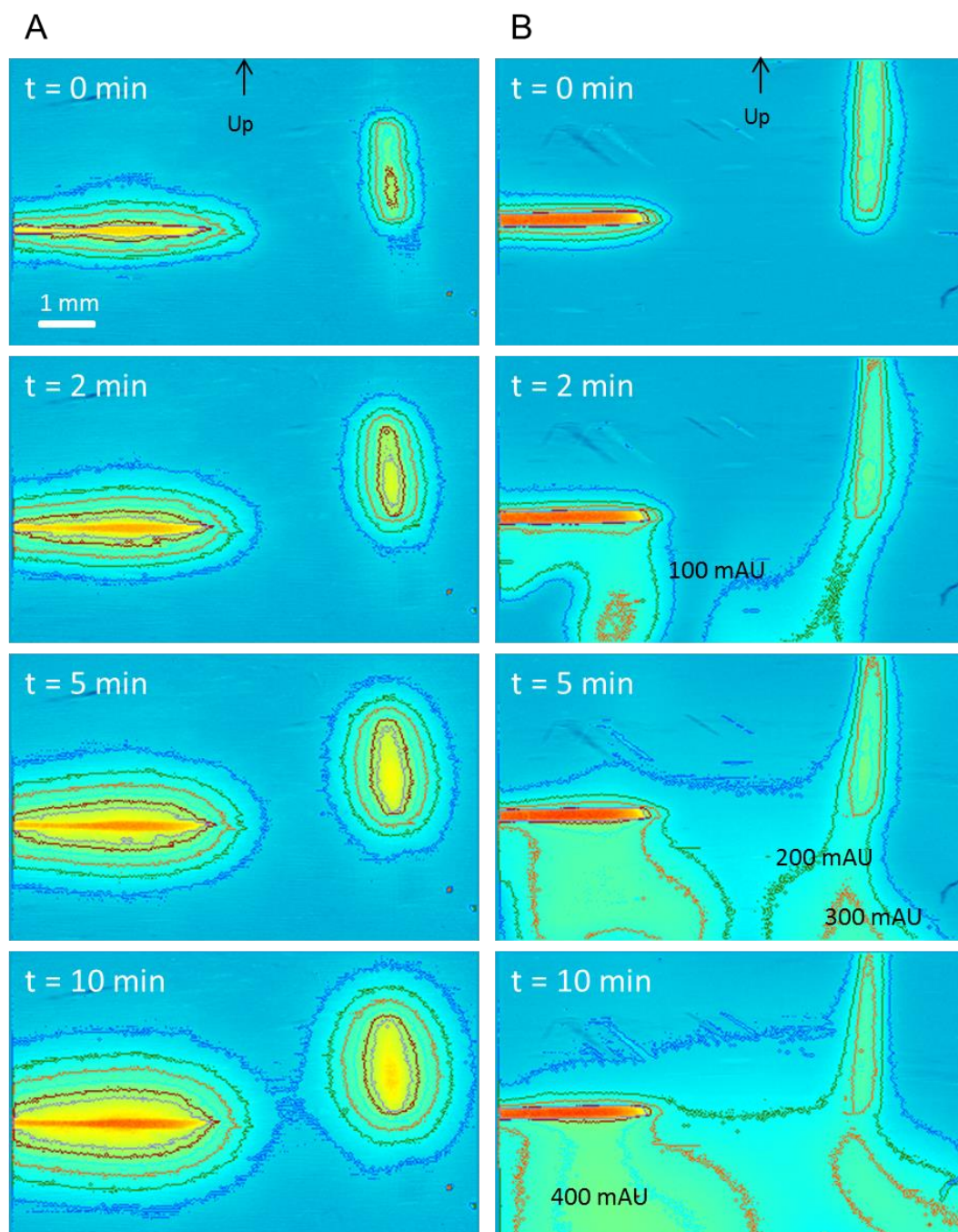


635
636 **Fig. 6.** Absorbance maps of the grids obtained by the ActiPix D100 UV Area Imaging (Paraytec
637 Ltd, York, UK) and Sirius SDI (Sirius Analytical Ltd, East Sussex, UK) imaging system with
638 pixels binned 1×1 at 610 nm, when the bar pattern grids (100 μm line width, 100 μm vacancy
639 before repeat) were placed on the cover slip of the sensor surface (A and B) and on quartz cells,
640 placing the grid 1.2 mm above the cover slip of the sensor surface (C and D). Images are $9.0 \times$
641 7.2 mm^2 and the absorbance values range between 0 mAU (dark blue) and ~ 1400 mAU (red).



642

643 **Fig. 7.** A) Microscope photograph (the image is $8.3 \times 6.4 \text{ mm}^2$) and B) absorbance maps of the
 644 lidocaine crystals arranged in a quartz cell obtained by the Sirius SDI imaging system with pixels
 645 binned 4×4 at 254 nm. The image is $10.4 \times 4.6 \text{ mm}^2$. C) Absorbance – y-distance profile of the
 646 lidocaine crystal placed in the x-direction (—) and absorbance – x-distance profile for crystal
 647 placed in the y-direction (—) for determining the width of the crystals from the absorbance maps
 648 and D) normalized absorbance - distance profile of one side of a lidocaine crystal placed in the x-
 649 direction (—) and y-direction (—) for estimating the resolution of the Sirius SDI imaging
 650 system.



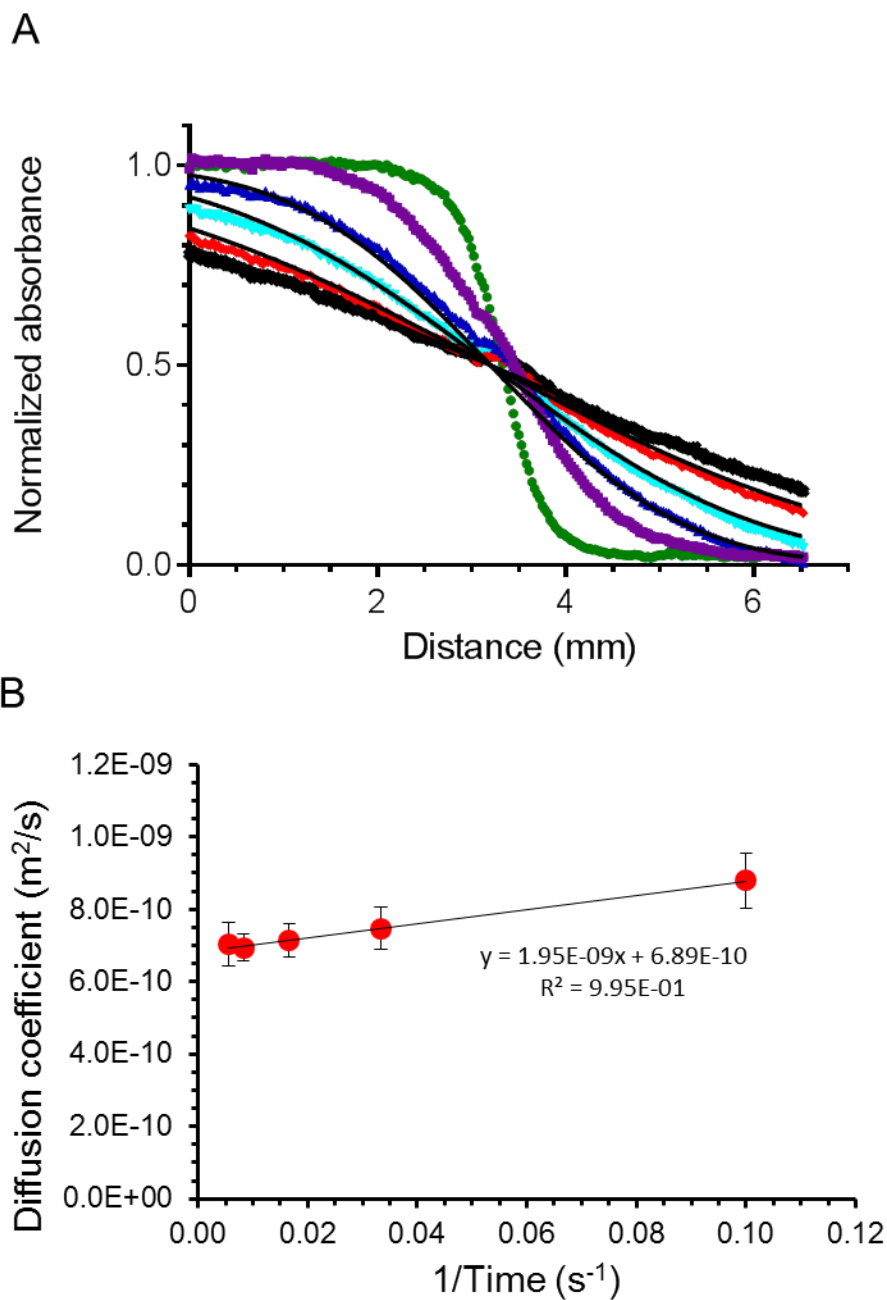
651

652 **Fig. 8.** Time-dependent absorbance contour maps of the dissolution of lidocaine crystals in A)

653 0.5% (w/v) agarose gel, pH 7.4 and B) 0.067 M phosphate buffered solution, pH 7.4. The

654 dissolution was performed in quartz cells with 1 mm light path using the Sirius SDI UV imaging

655 system with the pixels binned 4×4 at 254 nm and the sensor head placed in the upright position.



656

657 **Fig. 9.** A) Absorbance – distance profiles for lidocaine diffusion in 0.5% (w/v) agarose hydrogel
 658 matrix, pH 7.4, after 0 (●), 10 (■), 30 (▲), 60 (▼), 120 (◆) and 180 min (+) obtained using the
 659 Sirius SDI system. The black lines represent the fits to Eq. (1). B) Fitted diffusion coefficients of
 660 lidocaine in 0.5% (w/v) agarose hydrogel matrix, pH 7.4, as a function of the inverse of time.